

# Adaptive Airfoil Dynamic Stall Control

Michael Kerho\*

Rolling Hills Research Corporation, 420 N. Nash St., El Segundo, CA 90245  
mike@rollinghillsresearch.com

## Abstract

This paper will document research being performed under an SBIR Phase II program funded by the Army Aeroflightdynamics Directorate at NASA Ames research center. The purpose of this study is to investigate an adaptive airfoil design to alleviate, or greatly reduce the negative effects of dynamic stall on rotorcraft blades. The adaptive airfoil design uses compliant structures technology to design an aerodynamically smooth, variable droop leading-edge for airfoil dynamic stall control. Compliant structures technology coupled with variable camber leading-edge dynamic stall control has the potential to significantly improve the performance of modern rotorcraft. The research presented here will focus on the numerical predictions of the aerodynamic performance of the adaptive leading-edge. Both steady and unsteady time accurate numerical predictions for a 2-D pitching and deforming airfoil were performed using a modified version of the Navier–Stokes solver OVERFLOW. The OVERFLOW code was modified to allow for a dynamically deforming grid system. In addition to the dynamic pitch and deformation capability, the OVERFLOW code was modified to allow for a variable Mach number throughout the pitch cycle. The varying Mach number is used to more closely mimic the rotational behavior of the rotorcraft blade in forward flight. Numerical simulations were obtained with increasing complexity: from a simple fixed Mach number with a sinusoidal pitch cycle through a prescribed CAMRAD II pitch distribution with fully variable Mach and a dynamically deforming airfoil. Results obtained to date indicate that the variable droop/camber compliant leading-edge system can achieve a higher  $C_{lmax}$  than a baseline section, or eliminate the dynamic stall vortex at a  $C_l$  equivalent to the baseline section  $C_{lmax}$  while maintaining the baseline section's high Mach number advancing blade characteristics.

## Nomenclature

$c$	Airfoil chord length
$C_l$	Lift coefficient, $L/0.5\rho U_\infty^2$
$C_d$	Lift coefficient, $D/0.5\rho U_\infty^2$
$C_m$	Pitching moment coefficient, $M/0.5\rho U_\infty^2 c$
$k$	Reduced frequency, $\omega c/2U_\infty$
$M_\infty$	Freestream Mach number
$r$	Rotor blade radial coordinate
$R$	Rotor blade radius
$U_\infty$	Freestream velocity, ft/s
$\alpha$	Angle-of-attack, $^\circ$
$\mu$	Advance ratio, $M_\infty/M_{tip}$
$\omega$	Pitch rate, rad/s
$\psi$	Rotor azimuth, $^\circ$ (0 aft)

---

\* Chief Aerodynamicist, AIAA Associate Fellow

## Introduction

For fixed wing aircraft, wing stall limits the low speed characteristics of the aircraft. For rotorcraft, however, retreating blade stall is the primary limiting factor affecting the high-speed characteristics and payload capability of the aircraft. During forward flight, the advancing rotor blade encounters increased velocity due to the combination of the rotational velocity of the rotor combined with the rotorcraft's forward speed. Conversely, the retreating blade experiences a decreased velocity. In order to maintain level, coordinated flight, the lift generated from the retreating blade must equal that of the advancing blade. In order to achieve balanced lift across the rotor disk as speed increases, the angle-of-attack of the retreating blade must increase due to its lower relative velocity. Simultaneously, the advancing blade has a higher relative velocity and must decrease in angle-of-attack to maintain constant lift. At some forward speed, the increasing angle-of-attack of the retreating blade will cause it to stall. The tendency for the retreating blade to stall in forward flight is inherent in all present day rotorcraft and is a major factor in limiting their forward speed and maneuverability.<sup>1</sup> The retreating blade stall causes buffeting and vibration at critical airspeeds. Large negative pitching moments are also observed. Because the blades are normally flexible, the pitching moment change also poses aeroelastic problems. Figure 1 shows a representative schematic of the angle-of-attack and stall distribution for a typical rotorcraft blade system in forward flight.

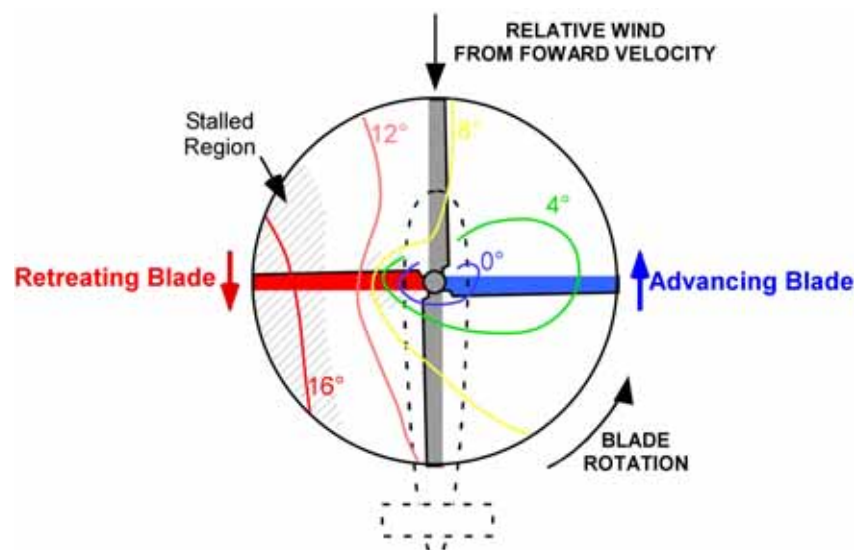


Figure 1: Angle-of-Attack and Stall Distribution in Forward Flight<sup>1,2</sup>

In addition to the essentially static stall of the retreating blade at higher forward velocities, the dynamics of the pitching blade introduce additional problems. When an airfoil is pitched up rapidly, as it does as the blade rotates from the advancing side to the retreating side, it is possible to over-shoot the static  $C_{l_{max}}$  and achieve a significantly higher  $C_{l_{max}}$  (Dynamic). In addition, when the airfoil is then pitched back down, or held at a constant angle-of-attack, there is a corresponding decrease in lift that extends below the static value. The characteristic lift overshoot has been observed in both fixed wing and rotary wing aircraft for many years. For the case of a traditional airfoil, an overshoot above the static  $C_{l_{max}}$  occurs in the pitch cycle due to the formation of a large vortex on the airfoil upper surface that separates and travels downstream. The final breakdown in  $C_l$  for the section occurs when this vortex has traveled past the trailing-edge. At this point the flow is massively separated and the lift drops to levels far below those typical of the static curve, requiring a significant reduction in angle-of-attack before reattachment. The movement of the vortex, or dynamic stall vortex, from the airfoil leading to trailing-edge results in a large change in section pitching moment, becoming increasingly negative (nose-down) as the vortex reaches the

trailing-edge. While the dynamic lift provides a benefit in  $C_{lmax}$ , the more severe stall that follows further limits the performance of the helicopter blade system.

Many avenues have been explored in an attempt to overcome the limitations imposed by retreating blade stall. Airfoils are selected to provide high lift, low drag and a near zero pitching moment to reduce control moments. The blade tips are often twisted, or washed-out, to provide lower angles-of-attack at the tips. The airfoil section itself can be varied across the blade span to smooth out the lift distribution. Generally, a trade off is made between the performance of the advancing blade versus the retreating blade. Variable geometry airfoils are a good method of optimizing the airfoil shape for the local flow conditions as the blade rotates. These variable shape/camber sections have proven effective in both experimental and numerical studies.<sup>3,4,5,6,7</sup> For a rotorcraft application where the airfoil is pitched up in angle-of-attack, the leading or trailing-edge of the airfoil is dynamically deformed at different angles of incidence. The new deformed airfoil shape is better able to deal with the large adverse pressure gradients created by the suction peak generated by the high section incidence. Dynamically drooped leading-edges have been shown to significantly reduce or eliminate the massive flow separation and the dynamic stall vortex for a given angle-of-attack condition.<sup>6</sup> While experimental and computational results have shown great promise for variable camber geometries, traditionally variable geometry airfoils, such as the Mission Adaptive Wing (MAW)<sup>8</sup> have been very complex structurally and consequently heavy and maintenance intensive and are not appropriate for the confined space requirements and harsh operating environment of a rotor blade. Another significant challenge for a variable camber rotor section is the fact that the camber change must happen cyclically with the blade rotation. This periodic change in the blade shape must occur on the order of 5 to 7 Hz. The severely constrained space requirements, coupled with the frequency of operation and high g rotational environment, have made a variable camber blade section impractical. Recent advances in the design of compliant smart structures technology, however, have made the possibility of a reliable and robust variable camber blade section that can operate at the required frequencies a reality.

The purpose of the current project is to attempt to exploit the aerodynamic benefits associated with deformable compliant structures to produce a variable camber leading-edge for dynamic stall control. Although the current project is a multidisciplinary design approach, coupling the structural and aerodynamic design, only the numerical simulations involved in the aerodynamic design will be discussed here.

## Geometry

The baseline airfoil used in this study is the Sikorsky SSC-A09 section. The SSC-A09 is representative of a modern rotorcraft blade section which performs well at transonic conditions but could use some reshaping for better dynamic stall performance. One of the key aspects of the current study was to produce a structurally realistic aerodynamic design. Since most modern rotorcraft blade sections have a D-spar located at the leading-edge of the airfoil, this D-spar must be moved aft in order to allow space for the deformation mechanism. From a stiffness and balance point of view, the aft movement of the D-spar must be minimized. There must be sufficient space in front of the D-spar, however, to provide for a reasonable camber change and droop deflection to maximize the aerodynamic benefit. One of the designs studied drooped the leading-edge 10° downward while moving the D-spar aft to the 8.5% chord location. The section is termed the Spar85Defl10. A schematic of the baseline and drooped SSC-A09 section is shown in Figure 2. The actual deformation begins at approximately the 15% chord location. The structure is designed to continuously deform throughout the pitch cycle at a rate up to 7Hz.

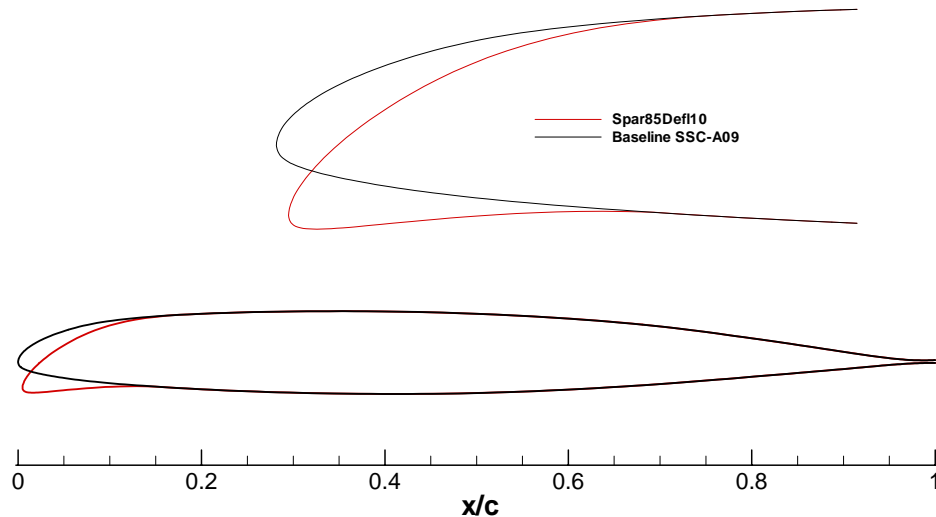


Figure 2: Comparison of the Baseline SSC-A09 and a  $10^\circ$  compliant drooped Spar85Defl10 section.

## Numerical Methodology

Several compliant variable camber leading-edge designs have been studied numerically, both statically and dynamically. The compressible Reynolds-averaged Navier-Stokes computational fluid dynamics code OVERFLOW has been used for the numerical predictions in this study. The OVERFLOW code uses chimera overset (structured) grid systems and has been developed at NASA and applied to a wide range of both internal and external fluid dynamic problems. The OVERFLOW 1.8ab code was extensively modified to include the dynamically deforming grid and variable Mach capability. All analysis performed to date has been 2-D using a single c-mesh grid.

A grid refinement study for the time accurate simulations produced a grid with dimensions of  $377 \times 93$  and a  $y^+$  of the first grid line off the surface on the order of 1. In order to resolve the time dependent features of the flow field with sufficient accuracy and proper computational convergence, approximately 30,000 time steps per oscillation were used with 3 Newton sub-iterations. The use of up to 6 Newton sub-iterations was also investigated but found to provide identical results to the 3 sub-iterations. Solutions were run for a period of 2.5 cycles to provide sufficient periodic convergence. All cases were run fully turbulent using Roe upwinding and the Spalart-Allmaras turbulence model.

## Grid Deformation

The deforming grid capability allows the leading-edge of the airfoil to droop dynamically throughout the pitch cycle providing a more realistic performance prediction. Several routines within OVERFLOW were extensively modified to include the deformation routines. Additionally, a new input deck has been added to the OVERFLOW code to allow the unsteady input variables (reduced frequency, pitch amplitude, droop schedule, etc...) to be specified in the input file. Through the input deck, the routines can be specified to use a simple sinusoidal pitch cycle, or a user supplied pitch cycle can be specified ( $\alpha$  versus  $\psi$ ) and read in during start-up. Similarly, the surface deformation is handled in the same manner. A simple sinusoidal deformation scheme with specified limits and chordwise extents, or a user supplied deformation schedule can be read in during start-up.

The deforming grid capability added to the OVERFLOW code is rather generic and robust in that the method could be rather easily extended to a 3-D or multi-grid system. In order for the deforming grid capability to be easily extended to 3-D or a multi-grid overset system, it would be beneficial for some cases to avoid having to recalculate the inter grid connectivity after every grid deformation. It would be more

desirable to allow individual grids to deform while maintaining their outer boundary without any movement of the overlap regions. This type of deformation strategy was employed in the current study. The method is similar to and was modeled after that proposed by Morton, Melville, and Visbal<sup>9</sup> with modifications made to handle a c-mesh.

The most common grid or mesh deformation strategy in use is trans-finite interpolation (TFI). TFI is popular due to its algebraic nature and low computational cost. TFI schemes may be as simple as connecting surfaces with straight lines in the body normal direction and preserving arc-length between nodes or more usually a simple linear distribution of translational displacements.<sup>9</sup> The drawback in using a TFI scheme is that generally they do not guarantee grid orthogonality at the body surface, a desirable quality for Navier-Stokes viscous flow simulations. The strategy developed by Morton et al.<sup>9</sup> is similar to TFI in that its approach in redefining the normal grid lines is algebraic. Grid quality and orthogonality of the mesh at the surface, however, is maintained. The approach also limits deformation to a specified region of the grid, allowing the outer far field regions to be held fixed, maintaining overlap and connectivity. The strategy is relatively robust and allows for large surface deformations.

From Morton et al.<sup>9</sup>, for an initial grid and surface displacement, the translation and rotation of each surface node is computed from the deformed aerodynamic surface. Each normal grid line is then moved in a rigid-body fashion according to the displacement and rotation of the surface node to form a reference, displaced grid line. The new grid line is then constructed by blending the reference grid line and the undeformed grid line. A cubic blending with zero slope at the end point assures both that any initial wall orthogonality or grid quality is maintained and that the grid transitions smoothly in the far field. This method of grid deformation is used to deform the leading-edge area of the airfoil and also for changes in angle-of-attack for all dynamic solutions. An example of the SSC-A09 grid undergoing a leading-edge deflection from 0° to 10° droop for  $\alpha$ 's from 0° to 20° is shown in Figure 3. From Figure 3, the deformation routine produces a smooth transition throughout the deformation. Most importantly, however, is that the grid mesh orthogonality is maintained at the surface for each grid.

Due to the deforming nature of the grid, use of the Geometric Conservation Law (GCL)<sup>10</sup> in the flow solver was also investigated. In order to maintain global conservation for fluid dynamic numerical solutions involving body conforming coordinate transformations, spatial and temporal grid metrics must satisfy certain geometric identities.<sup>11,12</sup> If the GCL is not satisfied, inaccuracies and or instabilities in the solution may result. Modifications were made to the OVERFLOW code to satisfy the GCL and time accurate fully deforming cases were run with and without GCL to determine its effect. While being the most correct form of the numerical solution, inclusion of the GCL in the flow solver produced results that were within plotting accuracy when compared to solutions generated without the GCL implementation. This is most likely a result of the small time steps used coupled with the fact that the basic OVERFLOW formulation includes free-stream subtraction. Since no noticeable differences were observed between the baseline and GCL implementation, GCL was not used due to its additional computational cost.

### **Unsteady Mach Capability**

In addition to the deforming grid capabilities of the modified code, the ability to vary the Mach number throughout the pitch cycle has been added to the modified OVERFLOW code. The varying Mach number will more closely mimic the rotational behavior of the rotorcraft blade in forward flight. A rather simple and elegant solution was arrived at for varying the Mach number. Instead of physically moving the grid to simulate the varying speed of the rotating blade, the time metric for the grid was modified. By modifying the time metric for the grid, the code sees a variation in grid speed without the grid actually moving. As a result, the grid boundaries remain constant, but the surface appears to be moving. Instead of the reference system where the body remains fixed in space and flow moves, the code thinks the body is translating in the direction of the free-stream flow, producing an additive velocity to the free-stream.

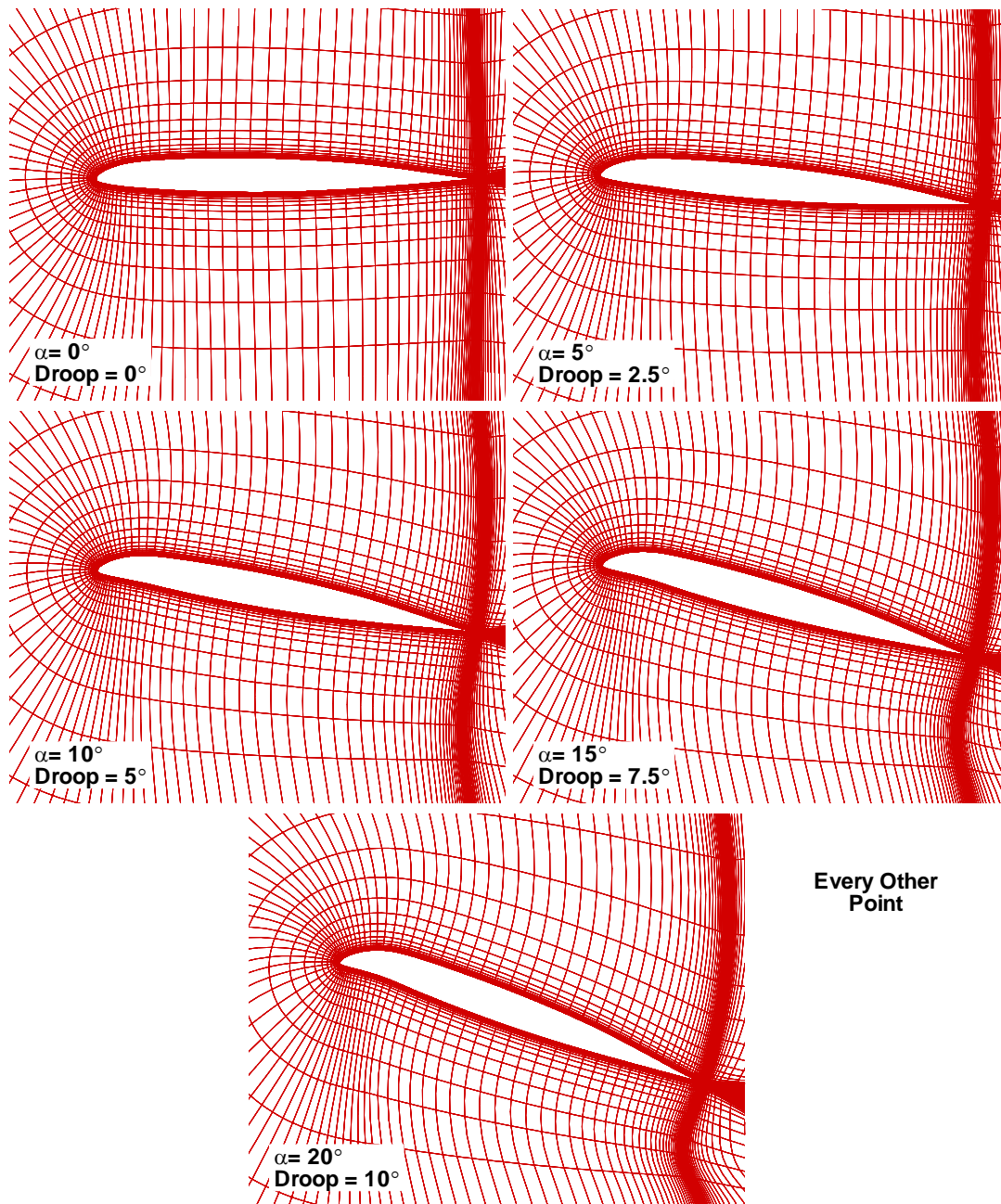


Figure 3: Example showing progressive grid deformation for the SSC-A09 section undergoing a  $0^\circ$  to  $10^\circ$  nose droop during a pitch cycle from  $0^\circ$  to  $20^\circ$  angle-of-attack.

Several test cases were run to verify modified Mach number capability. For example, the baseline SSC-A09 section was run statically at  $\alpha=0^\circ$ ,  $M_\infty=0.70$  and compared to a time accurate varying Mach number case with an equivalent free-stream Mach number. For the equivalent Mach number case, a fixed free-stream Mach number of  $M=0.4$  was used with a varying component of  $0.3$ , yielding a total Mach number of  $M=0.70$ . The pressure distributions for these two cases are shown in Figure 4. From Figure 4, the two pressure distributions are identical. The modified code correctly accounts for the added Mach number capability in both the flow solver and reduction routines.

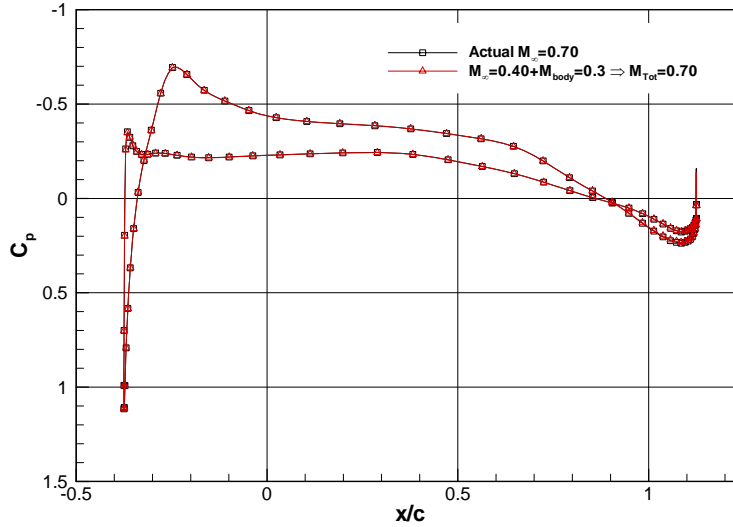


Figure 4: Comparison of baseline OVERFLOW surface pressure results and results generated using the varying Mach capability for the baseline SSC-A09,  $\alpha=0^\circ$ .

**Numerical Validation**

In order to provide some validation of the modified OVERFLOW results, numerical and experimental unsteady results for the NACA 0012 are compared. The experimental results are those of Wood<sup>13</sup> for a sinusoidal pitch cycle,  $\alpha=6.25^\circ+8.5^\circ\sin(\omega t)$ . Unsteady experimental and OVERFLOW lift curve and pitching moment results for the NACA 0012 section at a reduced frequency of  $k=0.075$ ,  $M=0.40$ , and  $Re=3.4 \times 10^6$  are shown in Figure 5. From Figure 5, the  $C_l$  results compare relatively well with the measured data. Lift levels on the up stroke are slightly under predicted, but  $C_{lmax}$  and the angle at which it occurs are in good agreement. OVERFLOW also predicts lower lift on the downstroke until reattachment. From the pitching moment results, OVERFLOW over predicts the magnitude of the negative pitching moment due to the passage of the dynamic stall vortex. Overall, the unsteady time accurate OVERFLOW results compare relatively well with the experimental data.

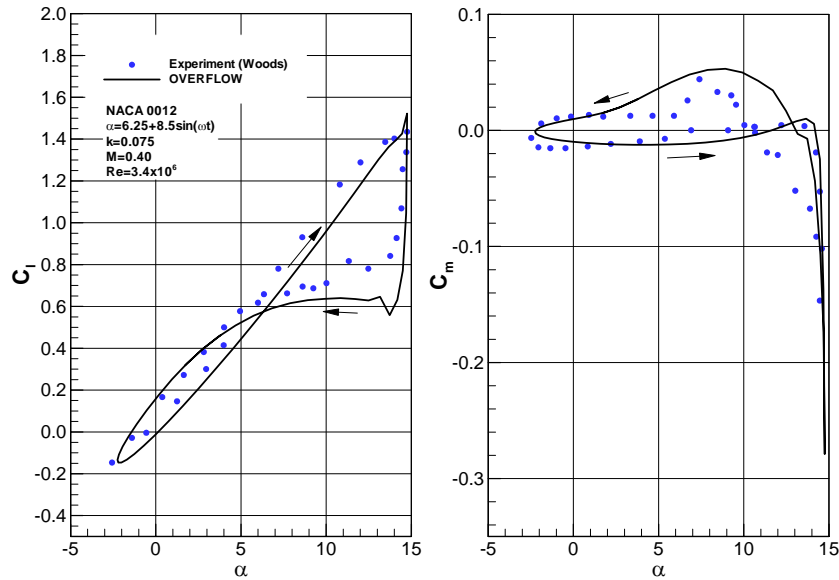


Figure 5: Comparison of forced oscillation time accurate OVERFLOW and experimental data for a NACA 0012,  $k=0.075$ ,  $M=0.40$ , and  $Re=3.4 \times 10^6$ .

## Results

Unsteady time accurate results for the baseline SSC-A09 and compliant adaptive Spar85Defl10 sections will be presented in two groups. The first group represents traditional sinusoidal forced oscillations at a fixed Mach number. The second group of results represents a more realistic rotorcraft blade environment. Instead of the sinusoidal pitch oscillation, both the pitch and Mach history are prescribed as a function of the blade rotation angle,  $\psi$ . The pitch history is derived from comprehensive rotorcraft analysis results obtained from a CAMRAD II analysis of a UH-60A Blackhawk helicopter. This more realistic pitch history is coupled with a variable Mach number which more closely mimics the rotational behavior of the rotorcraft blade in forward flight.

### Sinusoidal Oscillations

Dynamic lift curve results for the baseline SSC-A09 section and the compliant adaptive section (Spar85Defl10) undergoing a sinusoidal pitch cycle with  $\alpha=10^\circ+10^\circ\sin(\omega t)$ ,  $k=0.075$ ,  $M=0.40$  are shown in Figure 6. The droop schedule for the compliant adaptive section was  $\alpha_{\text{droop}}=5^\circ+5^\circ\sin(\omega t)$ . From Figure 6, the difference in the dynamic results between the baseline SSC-A09 section and the drooped Spar85Defl10 section are dramatic. The baseline SSC-A09 section stalls at approximately  $17^\circ$  with a  $C_{l\text{max}}=1.9$ , followed by increasing separation with increasing  $\alpha$ . The variable camber section, however, doesn't stall until approximately  $19.5^\circ$  with a  $C_{l\text{max}}$  of 2.1. The character of the stall is also different. The baseline SSC-A09 section  $C_{l\alpha}$  increases in slope before reaching  $C_{l\text{max}}$ , whereas the adaptive section  $C_l$  reaches a slight plateau before increasing sharply just prior to reaching its  $C_{l\text{max}}$ . These differences are due to the nature of the separation. For the SSC-A09 section, the separation is shock induced and begins near the leading-edge. The increase in slope prior to  $C_{l\text{max}}$  is the formation and shedding of the dynamic stall vortex. For the variable camber section, however, separation begins at the trailing-edge and moves forward before a vortex forms. The slight plateau in  $C_l$  before increasing prior to  $C_{l\text{max}}$  is the onset of trailing-edge separation. The sharp increase in  $C_l$  is due to the vortex that forms and sheds as separation moves quickly forward. These differences in stall characteristics also effect the drag and pitching moment behavior. Both the drag and pitching moment results show markedly better behavior for the drooped section throughout the baseline SSC-A09 stall range. The large negative pitching moment and drag rise associated with the formation, shedding, and passage of the dynamic stall vortex is delayed well beyond the baseline SSC-A09. It should also be noted that the low  $\alpha$  upstroke behavior of the adaptive and SSC-A09 sections are identical. As a result, there should be no aerodynamic penalty incurred by the adaptive section on the advancing blade.

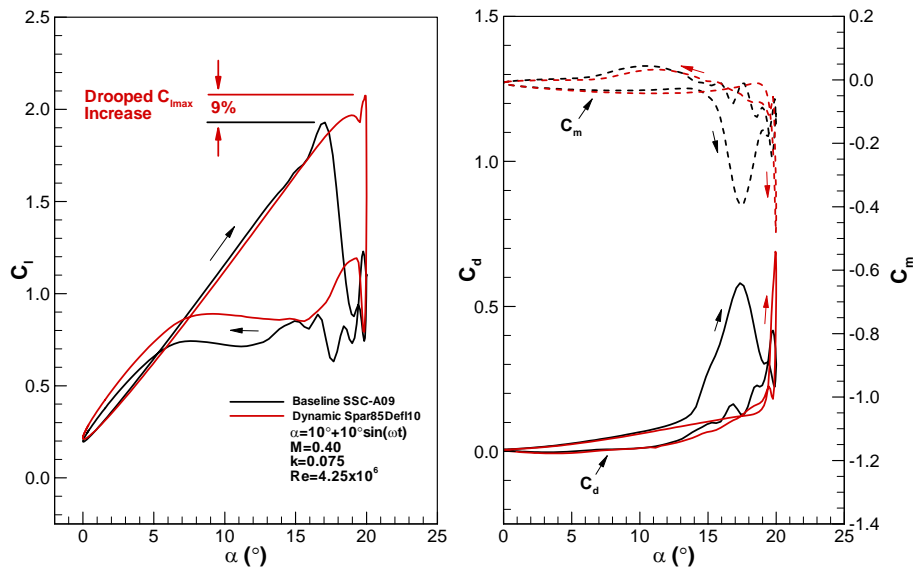


Figure 6: Comparison of force and moment polars for the SSC-A09 and Spar85Defl10 sections for a sinusoidal dynamic pitch loop,  $\alpha=10^\circ+10^\circ\sin(\omega t)$ ,  $k=0.075$ ,  $M=0.40$ .

From the dynamic results shown in Figure 6, the drooped geometry is clearly capable of providing an increased  $C_{lmax}$  and stall angle. The main objective, however, is to produce a section that can alleviate or eliminate the shedding of the dynamic stall vortex to an angle-of-attack and lift coefficient significantly higher than the baseline section. Since the previous results were run with a mean  $\alpha$  of  $10^\circ$ , with a  $10^\circ$  amplitude, the baseline and Spar85Defl10 section were re-run, limiting the max  $\alpha$  to  $17^\circ$ ,  $\alpha=8.5^\circ+8.5^\circ\sin(\omega t)$  to see if the shedding of the dynamic stall vortex could be eliminated. Pitch loop results for these cases are shown in Figure 7. From Figure 7, the  $C_l$  pitch loop results for the Spar85Defl10 section clearly show a marked difference from the baseline SSC-A09 section. The drooped section appears to completely eliminate the shedding of the dynamic stall vortex while maintaining the baseline section  $C_{lmax}$ . No large lift loss is observed during the downstroke. These results are confirmed by the drag and pitching moment behavior. The large drag rise and negative pitching moment associated with the shedding of the dynamic stall vortex on the baseline section are absent from the drooped section results. These results are very encouraging. Not only can the compliant variable camber section eliminate the negative drag and pitching moment effects associated with the dynamic stall vortex, it can do so without any loss in  $C_{lmax}$ .

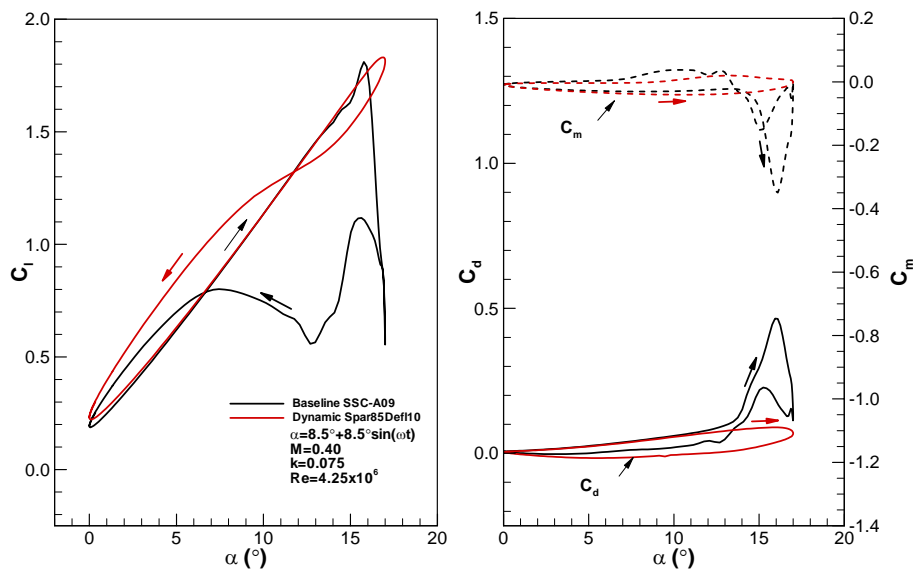


Figure 7: Comparison of force and moment polars for the SSC-A09 and Spar85Defl10 sections for a sinusoidal dynamic pitch loop,  $\alpha=8.5^\circ+8.5^\circ\sin(\omega t)$ ,  $k=0.075$ ,  $M=0.40$ .

Contours of Mach number for the baseline SSC-A09 and dynamically deformed section at different points throughout the pitch cycle are shown in Figure 8. From Figure 8, the separation and passage of the dynamic stall vortex for the baseline SSC-A09 section is clearly evident. The dynamically drooping Spar85Defl10 results, however, look markedly different. No large areas of reverse flow or formation of a dynamic stall vortex are observed. Also included in Figure 8 are contours of zero  $u$  velocity indicating regions of reverse flow. From Figure 8, large areas of reverse flow associated with the dynamic stall vortex are seen in the baseline section results. Again, the dynamically drooping Spar85Defl10 results look significantly different. Only a small amount of trailing-edge reverse flow at the pitch loop apex and initial down stroke are evident. The dynamically deforming section appears to provide significant aerodynamic benefits when compared to the baseline SSC-A09 section by eliminating the formation and passage of the dynamic stall vortex while producing a slight increase in  $C_{lmax}$ .

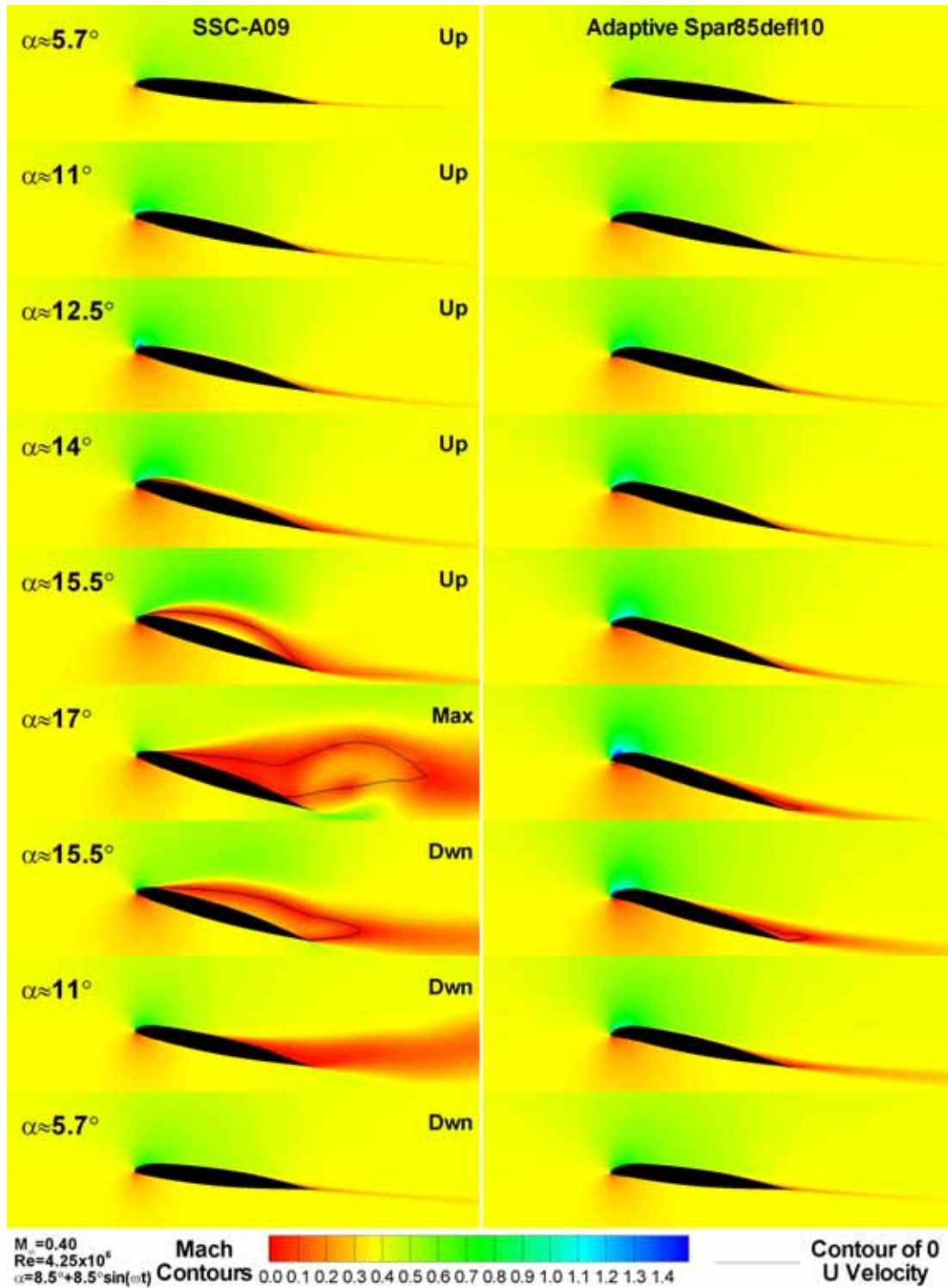


Figure 8: Mach contours for the baseline SSC-A09 and dynamically drooping Spar85Defl10 section at various  $\alpha$ 's throughout the pitch cycle,  $\alpha = 8.5^\circ + 8.5^\circ \sin(\omega t)$ ,  $k = 0.075$ ,  $M = 0.40$ .

## Prescribed Pitch/Mach History

In order to better understand the blade rotational effects and produce a more accurate aerodynamic prediction, prescribed pitch and Mach histories were investigated. The pitch and Mach effects were studied in increasing complexity. First the effect of a realistic pitch history was investigated as compared to the traditional sinusoidal variation. Next, the effect of a variable Mach number was added. The conditions for these unsteady runs simulate a heavy UH-60A operating at an advance ratio of  $\mu=0.33$ ,  $M_\infty=0.21$  at a blade radius of  $r/R=0.865$ . This advance ratio gives a blade rotational frequency of approximately 4.31Hz, slightly lower than the unsteady sinusoidal cases previously investigated (7.5Hz). The blade pitch history for the UH-60A case in question is that predicted by the comprehensive rotorcraft analysis code CAMRAD II<sup>14</sup> as determined by Bousman<sup>15</sup>. The lower rotational frequency results in a lower blade pitching reduced frequency (assuming a purely sinusoidal  $\alpha$  variation at a constant Mach number). With a varying Mach/ $\alpha$  distribution, however, the pitching reduced frequency varies continuously throughout the blade rotation, increasing rapidly during the retreating blade pitch-up.

In order to best study the effects of having a varying Mach/ $\alpha$  distribution, a set of unsteady runs were made where a constant Mach number with a sinusoidal pitch variation case is used as a baseline. This case is then compared against a case using constant Mach number with the CAMRAD II generated  $\alpha$  variation. Finally, these results are compared to a case where both the CAMRAD II generated  $\alpha$  schedule and variable Mach number are used. A comparison of the sinusoid/CAMRAD II  $\alpha$  schedules and constant/variable Mach as a function of blade rotation angle is shown in Figure 9.

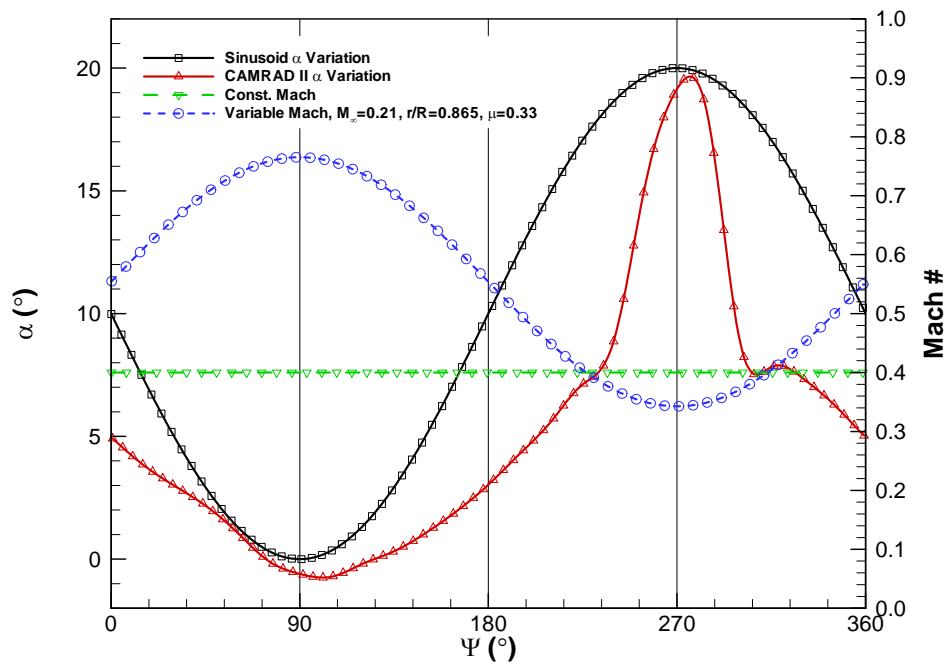


Figure 9: Comparison of sinusoid and CAMRAD II  $\alpha$  schedules and constant and variable Mach with blade rotation angle.

From Figure 9, both the sinusoid and CAMRAD II  $\alpha$  schedules reach a minimum  $\alpha$  around  $\Psi=90^\circ$  on the advancing side. As the blade rotates toward the retreating side the sinusoid continues a smooth increase in incidence while the CAMRAD II schedule increases at a much lower rate until approximately  $\Psi=230^\circ$  where the  $\alpha$  increases rapidly, followed by an equally sharp descent. For the majority of the pitch cycle, the CAMRAD II schedule has an effectively lower reduced frequency than the sinusoidal variation, with the exception being the rapid variation beginning at  $\Psi=230^\circ$  where the reduced frequency is higher

than the sinusoid schedule. Since the blade rotational velocity is constant, the Mach variation with blade rotation is sinusoidal and 180° out of phase with the  $\alpha$  schedule.

Force and moment results for the baseline sinusoidal  $\alpha$  with constant Mach, the CAMRAD II  $\alpha$  with constant Mach, and the CAMRAD II  $\alpha$  with variable Mach are shown in Figure 10. From Figure 10, the difference between the sinusoidal  $\alpha$  and CAMRAD II generated  $\alpha$  schedules for a constant Mach number are quite significant. The sinusoidal case reaches a  $C_{lmax}=1.77$  at  $\alpha=15.5^\circ$ , with the CAMRAD II case reaching  $C_{lmax}=2.05$  at  $\alpha=18.4^\circ$ . The increased reduced frequency generated by the rapid  $\alpha$  increase delays the separation of the dynamic stall vortex to a higher  $\alpha$ , producing a significantly higher  $C_{lmax}$ , accompanied by a larger loss in lift on the down stroke. The effect of the variable Mach number is also significant, producing a higher  $C_l$  on the up stroke and a further increase in  $C_{lmax}$ . The increased  $C_l$  on the up stroke is due to compressibility effects as a result of the increased Mach number on the advancing blade, whereas the increase in  $C_{lmax}$  is again due to an effective further increase in reduced frequency due to the reduction in Mach number during the pitch up on the retreating blade.

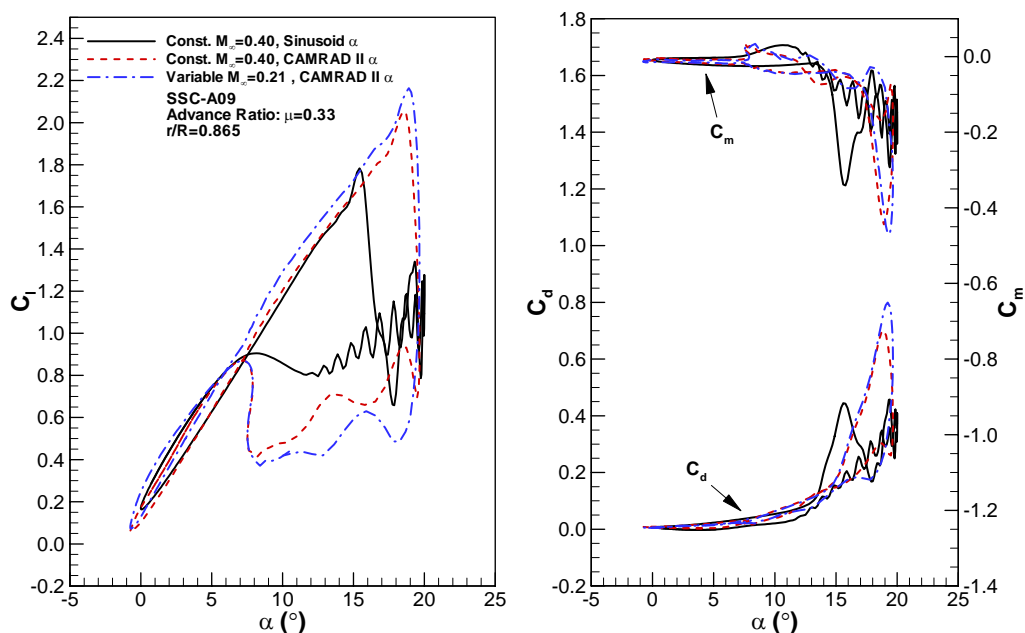


Figure 10: Comparison of unsteady results for the SSC-A09 section showing the effects of variable Mach and CAMRAD II  $\alpha$  distributions.

Unsteady contours of Mach number for the SSC-A09 with constant Mach and sinusoid pitch cycle are compared to the variable Mach and CAMRAD II pitch cycle in Figure 11. Also included in Figure 11 are contours of zero  $u$  velocity indicating regions of reverse flow. Recall from Figure 10, the constant Mach/sinusoid pitch case reaches its  $C_{lmax}$  at approximately  $15.5^\circ$ , whereas the variable Mach/CAMRAD II case reaches its  $C_{lmax}$  at  $19^\circ$ . From Figure 11, for both cases separation begins near the leading-edge due to a shock. Separation then extends aft in the form of a bubble which grows in size until shedding downstream. For the constant Mach/sinusoid case, separation begins at approximately  $12.5^\circ$ . Due to the increased pitch rate of the variable Mach/CAMRAD II case, separation onset is delayed until approximately  $15.4^\circ$ . The overall separation mechanism for both cases, however, appears to be similar. The increased pitch rate/reduced frequency of the variable Mach/CAMRAD II case simply delays the onset to a higher angle-of-attack.

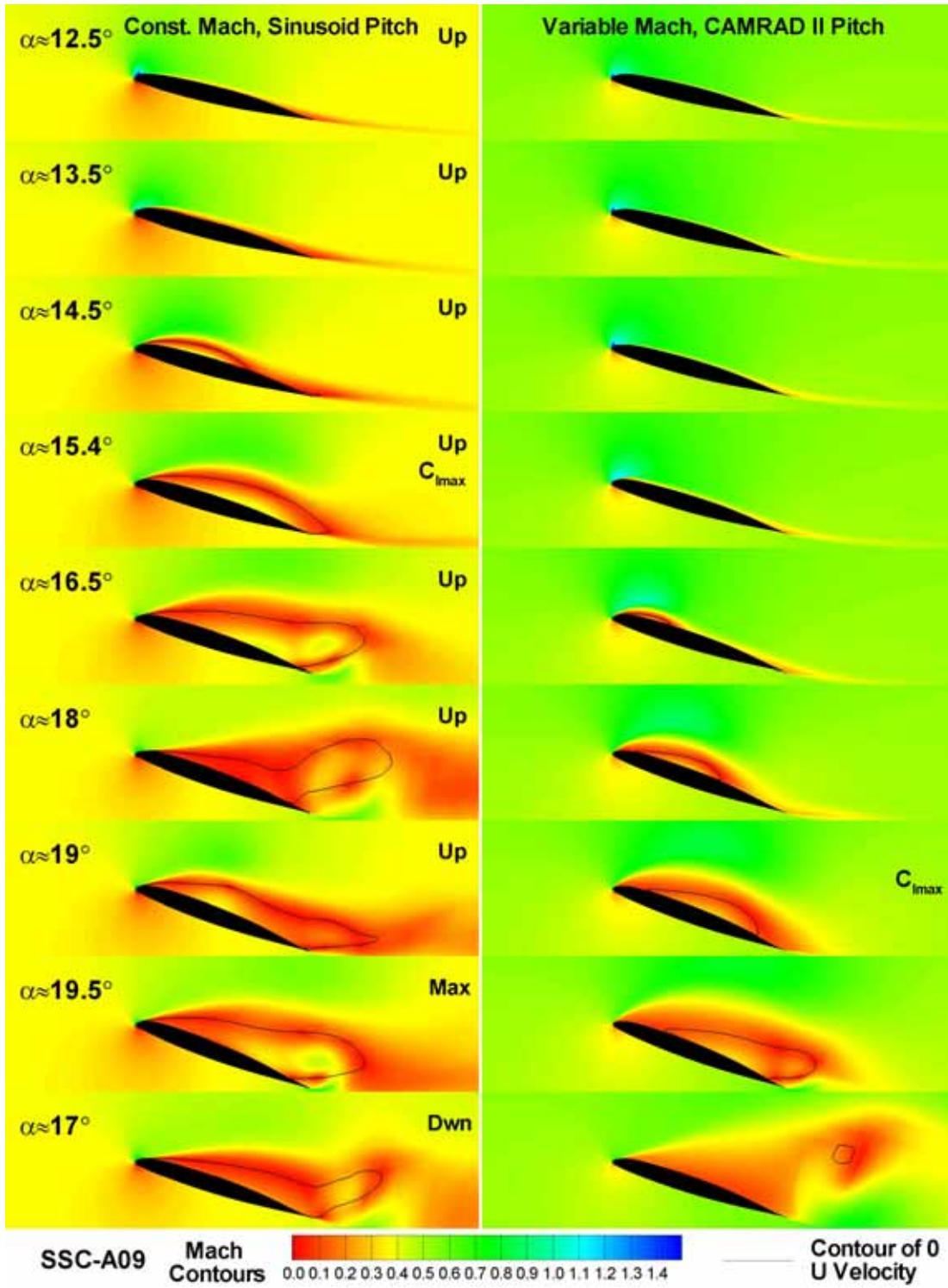


Figure 11: Unsteady Mach contours for the baseline SSC-A09 for a constant Mach, sinusoid pitch cycle and for the variable Mach CAMRAD II pitch cycle.

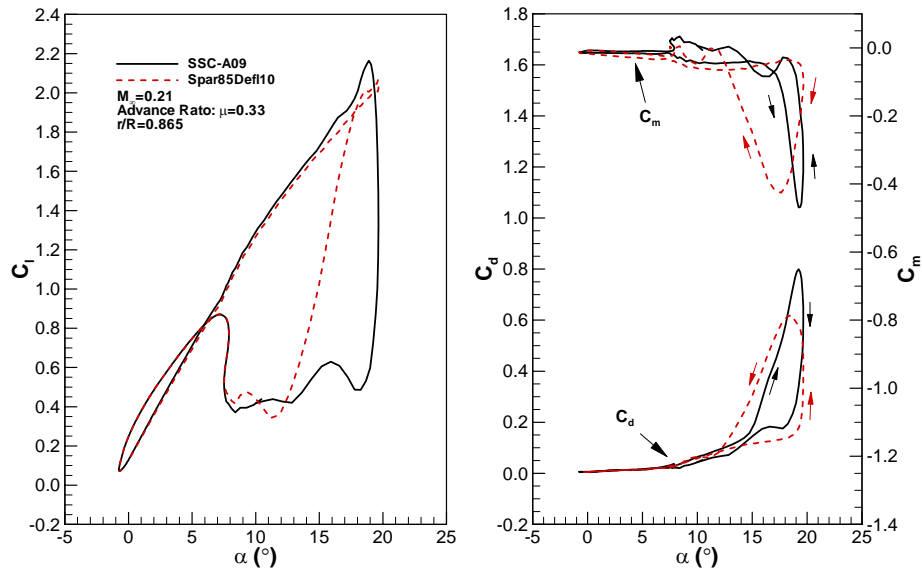


Figure 12: Comparison of unsteady results for the SSC-A09 and Spar85Defl10 sections for the variable Mach and CAMRAD II pitch cycle.

After running the baseline SSC-A09 section with the new Mach/ $\alpha$  schedules, the compliant droop geometry was investigated. The variable Mach/CAMRAD II pitch distribution results for the SSC-A09 section are compared to the adaptive airfoil Spar85Defl10 section results in Figure 12. The conditions shown in Figure 12 are again those for the UH-60A case,  $\mu=0.33$ ,  $M_\infty=0.21$  at a blade radius of  $r/R=0.865$ . Previous comparisons of the dynamic behavior between the SSC-A09 and the adaptive Spar85Defl10 section showed a higher  $C_{lmax}$  for the adaptive section. For the angle-of-attack range prescribed in the CAMRAD II pitch history, however, the SSC-A09 section is actually producing a slightly higher  $C_{lmax}$  than the adaptive section. The reasons for this role reversal will become evident shortly. The SSC-A09 section produces a higher  $C_{lmax}$  due to the fact that it's generating a much stronger, more pronounced dynamic stall vortex than the Spar85Defl10 section as evidenced by the  $C_d$  and  $C_m$  loops. Arrows denoting the pitch loop path for the SSC-A09 and Spar85Defl10 section are also included in Figure 12. Upon closer examination, the breaks in the  $C_d$  and  $C_m$  curves denoting the formation and passing of the dynamic stall vortex occur at a significantly lower  $\alpha$  for the SSC-A09 section as compared to the Spar85Defl10 section ( $\approx 15^\circ$  to  $17^\circ$  as compared to  $19.6^\circ$ ). The Spar85Defl10 section is clearly remaining attached longer and the larger  $C_{lmax}$  produced by the SSC-A09 section comes at the expense of increased drag and negative pitching moment at a lower  $\alpha$ . Unsteady contours of Mach number for the SSC-A09 and adaptive Spar85Defl10 section with the variable Mach and CAMRAD II pitch cycle are shown in Figure 13. Also included in Figure 13 are contours of zero  $u$  velocity indicating regions of reverse flow. The Mach and reverse flow contours shown in Figure 13 clearly show the SSC-A09 section generating a separation bubble near the leading-edge on the up stroke beginning at approximately  $\alpha \approx 15^\circ$  to  $17^\circ$ . The separation bubble grows in size with increasing pitch angle until it sheds near the max angle-of-attack. The adaptive Spar85Defl10 section, however, shows no reverse flow until the beginning of the down stroke. The higher  $C_{lmax}$  produced by the SSC-A09 section is solely a result of the shedding of the stall vortex at the pitch cycle apex. The adaptive section should be capable of remaining attached to a higher angle-of-attack and lift coefficient.

Finally, some slight further aerodynamic optimization of the upper surface leading-edge region of the Spar85Defl10 section was performed to determine if any further performance benefits could be obtained from the adaptive section. The new modified adaptive section is termed the Opt1 section. Like the Spar85Defl10 section, the Opt1 section also produces  $10^\circ$  of droop while moving the D-spar aft to the 8.5% chord location. Unsteady results for the SSC-A09, Spar85Defl10, and new Opt1 section for the variable Mach and CAMRAD II pitch cycle are shown in Figure 14. From Figure 14, the Opt1 results produce a  $C_{lmax}$  equivalent to the Spar85Defl10 section, but without the formation and separation of the dynamic stall vortex on the down stroke. No large reduction in  $C_l$  and increase in  $C_d$  or  $C_m$  are noted. The Opt1 section is an aerodynamically refined version of the Spar85Defl10 section. While both the SSC-A09

and Spar85Defl10 section produce a dynamic stall vortex for the  $\alpha$  range shown, the Opt1 section does not. The Opt1 section could therefore be pushed to a higher  $\alpha$  before a dynamic stall vortex is observed. As a result, the Opt1 section should theoretically have a higher  $C_{lmax}$  than the SSC-A09 and Spar85Defl10 sections with an increased pitch range.

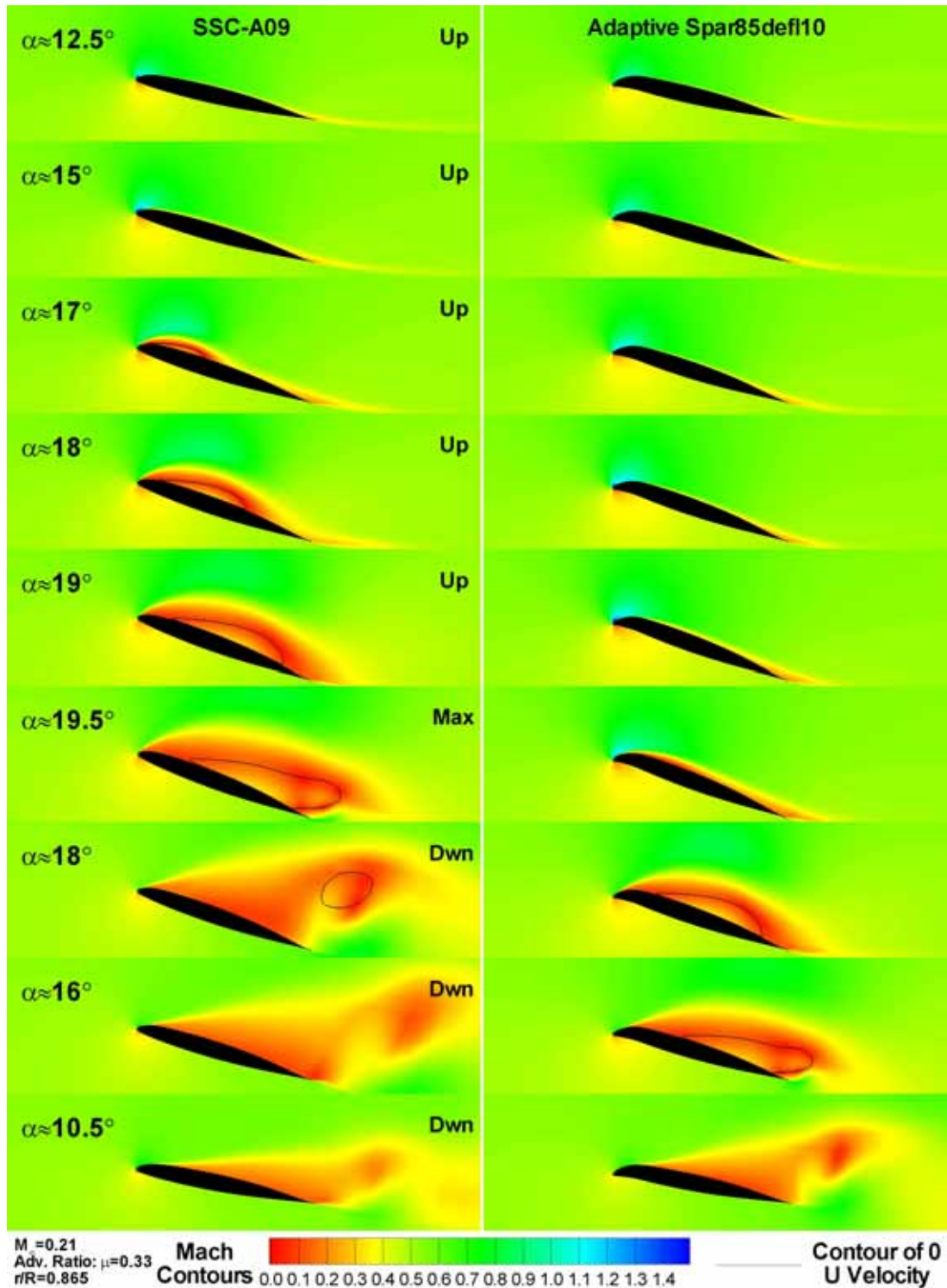


Figure 13: Unsteady Mach contours for the baseline SSC-A09 and adaptive Spar85Defl10 section for the variable Mach and CAMRAD II pitch cycle.

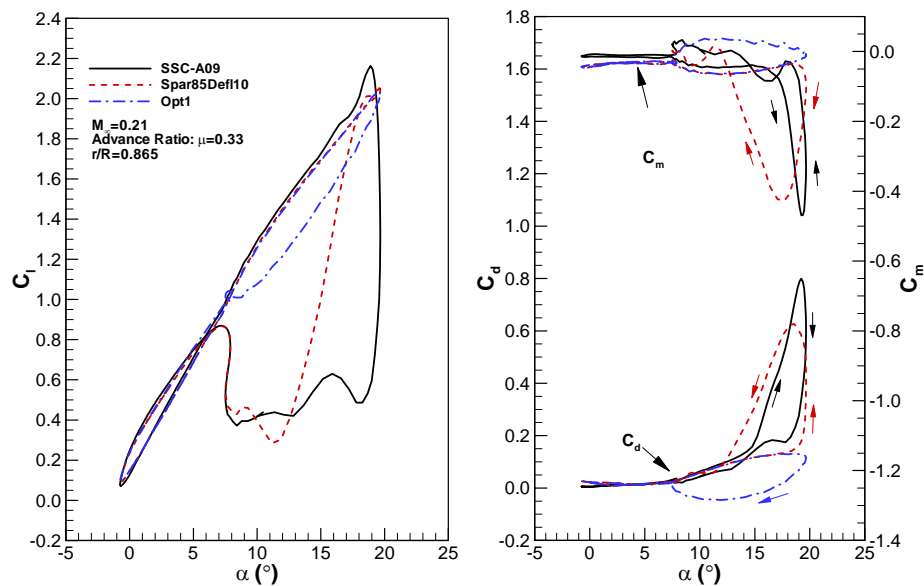


Figure 14: Comparison of unsteady results for the SSC-A09, Spar85Defl10, and Opt1 sections for the variable Mach and CAMRAD II pitch cycle.

The unsteady dynamic results presented for the Spar85Defl10 and Opt1 sections appear to be very promising from an aerodynamic standpoint. The variable Mach and prescribed CAMRAD II pitch cycle show results significantly different than that observed using the traditional constant Mach and sinusoidal  $\alpha$  variation. While still lacking the 3-D flowfield aspects of the finite rotor blade and blade/blade interactions, these more accurate representations of the blade environment provide a more accurate analysis tool than the traditional forced oscillation analysis.

## Conclusions

An adaptive variable camber airfoil designed to alleviate, or greatly reduce the negative effects of dynamic stall on rotorcraft blades has been investigated numerically. The variable camber airfoil is designed to deform dynamically in the form of a leading-edge nose droop throughout the rotorcraft pitch cycle allowing for an optimized blade section on both the advancing and retreating blades.

The OVERFLOW 1.8ab code was modified to include a dynamically deforming grid and variable Mach capability. These modifications allowed the baseline and adaptive rotor blade sections to be studied in a more realistic rotorcraft environment as compared to traditional forced oscillation analysis. The variable Mach capability simulates the rotational aspect of the rotorcraft flowfield in forward flight. In addition to the variable Mach number, a prescribed pitch cycle derived from CAMRAD II analyses were also investigated. The variable Mach/CAMRAD II pitch variation produced results significantly different than the traditional constant Mach/sinusoid pitch cycle forced oscillation.

Numerical predictions from this study have shown that the adaptive drooping design concept holds significant aerodynamic promise. Both the Spar85Defl10 and Opt1 sections were shown to significantly delay or eliminate the formation and shedding of the dynamic stall vortex as compared to the baseline SSC-A09 section. Results obtained to date indicate that the variable droop/camber compliant leading-edge system can achieve a higher  $C_{l_{max}}$  than a baseline section, or eliminate the dynamic stall vortex at a  $C_l$  equivalent to the baseline section  $C_{l_{max}}$  while maintaining the baseline section's high Mach number advancing blade characteristics. The significant challenge remains in the structural design and actuation of a realizable adaptive compliant rotor blade.

### Acknowledgements

This work was supported by the Army Aeroflightdynamics Directorate at NASA Ames research center under a Phase II SBIR award, contract number W911W6-04-C-0001. The author would like to thank the technical monitor Dr. Preston Martin for his support and many contributions throughout this program. The author would also like to thank Mark Potsdam of the Army Aeroflightdynamics Directorate for many conversations, suggestions, and insights concerning the black arts, and also for his GCL code subroutines. Finally, the author would also like to thank Dr. Pieter Buning of NASA Langley for his help and suggestions concerning the OVERFLOW code, and Dr. Joel Hetrick of FlexSys Corporation for his compliant surface deformation routines.

### References

- 1 Gessow, A and Myers, G., "Aerodynamics of the Helicopter," Frederick Ungar Publishing Co., New York
- 2 Prouty, R. W., "Practical Helicopter Aerodynamics," PJS Publications Inc., Peoria, Illinois.
- 3 Chandrasekhara, M., "Compressible Dynamic Stall Control Using a Shape Adaptive Airfoil," AIAA 99-0650, 37th AIAA Aerospace Sciences Meeting, Jan. 11-14, 1999, Reno, NV.
- 4 Geissler, W. and Sobieczky, H., "Dynamic Stall Control By Variable Airfoil Camber," AGARD, Aerodynamics and Aeroacoustics of Rotorcraft, Aug. 01, 1995.
- 5 Yu, Y. H., Lee, S., McAlister K. W., Tung, C., and Wang C. M., "Dynamic Stall Control for Advanced Rotorcraft Application," *AIAA Journal*, Vol. 33, No. 2, Feb. 1995.
- 6 Reuster, J. G., Baeder, J. D., "Leading Edge Deformation for Dynamic Stall Control," AIAA Paper 2001-0120, presented at the 39<sup>th</sup> AIAA Aerospace Sciences Meeting, Jan. 8-11, 2001, Reno, NV.
- 7 Fink, D.A., Hawkey, T.J., Gaudreau, M.P.J., Wellman, B., Ormiston, R.A., "An Electromagnetic Actuator for Individual Blade Control," American Helicopter Society 56<sup>th</sup> Annual Forum, Virginia Beach, VA, May 2-4, 2000
- 8 Advanced Fighter Technology Integration F-111 Mission Adaptive Wing, Proceedings of a symposium held at NASA Ames Research Center, April 1989. NASA CP 3055.
- 9 Morton, S. A., Melville, R. B., and Visbal, M. R., "Accuracy and Coupling Issues of Aeroelastic Navier-Stokes Solutions on Deforming Meshes," *AIAA Journal of Aircraft*, Vol. 35, No. 5, Sept. 98.
- 10 Thomas, P. D. and Lombard, C. K., "Geometric Conservation Law and Its Application to Flow Computations on Moving Grids," *AIAA Journal*, Vol. 17, No. 10, 1979.
- 11 Obayashi, S., "Freestream Capturing for Moving Coordinates in Three Dimensions," *AIAA Journal*, Vol. 30, No. 4, 1992.
- 12 Potsdam, M., Yeo, H., and Johnson, W., "Rotor Airloads Prediction Using Loose Aerodynamic/Structural Coupling," Paper presented at the American Helicopter Society 60<sup>th</sup> Annual Forum, Baltimore, MD, June 7-10, 2004.
- 13 Wood, M. E., "Results from the Oscillatory Pitch Tests on the NACA 0012 Blade Section," Aircraft Research Association, UK, ARA Memo 220, 1979.
- 14 Johnson, W., "Rotorcraft Aerodynamics Models for a Comprehensive Analysis," Paper presented at the American Helicopter Society 54<sup>th</sup> Annual Forum, Washington D.C., May 20-22, 1998.

---

<sup>15</sup> Bousman, W. G., "Airfoil Design and Rotorcraft Performance," Paper presented at the American Helicopter Society 58<sup>th</sup> Annual Forum, Montreal, Canada, June 11-13, 2002.